nature physics

Supplementary information

https://doi.org/10.1038/s41567-025-02874-0

Observation of polarization density waves in $SrTiO_3$

In the format provided by the authors and unedited

THz Pump Field Spectrum

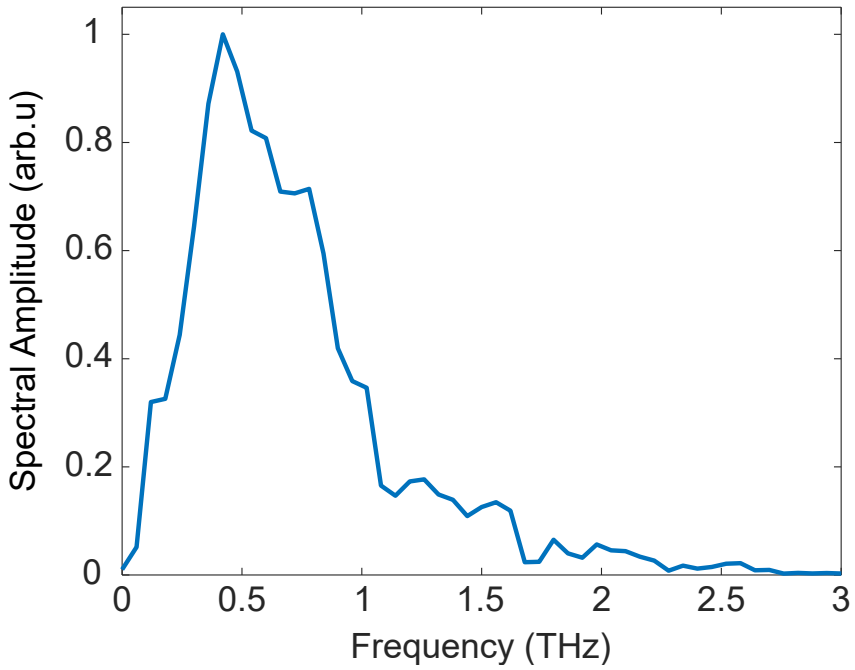

Fig. S1: **THz pump field spectrum.** Fourier transform of the upper crystal electro-optic sampling trace shown in the main text Fig. 2a.

Identifying Twin Domains

Upon cooling below the structural phase transition at $T = 105K$, an antiferrodistortive (AFD) instability induces a low-symmetry tetragonal phase in $SrTiO_3$ [1, 2]. The distortion can develop along any of the three equivalent cubic crystallographic directions, leading to the formation of three potential twin domains. As a result, the Bragg reflections separate into three distinct peaks, originating from the different domains illuminated by our x-ray probe. In Fig. **S2**a we show the detector image of the x-ray scattering, with the sample oriented close to the nominal (3,3,3) reflection. Two distinct features appear in the image, marked by a red square and a green square. In Fig. **S2**b we present the integrated intensity of these features versus the angle of one of the sample rotation motors exhibiting three distinct peaks corresponding to the three different orientational domains. To identify the orientation of the twin responsible for each peak we use the measured $SrTiO_3$ lattice constants [3], distinguishing between the three twins by directing the long axis along the three crystallographic directions and calculating the (3,3,3) Bragg reflection for each orientation. We compare the diffraction direction and sample orientation of the calculated reflections to those of the experimental peaks in Fig. **S2**b. Peak 1

is identified with a domain where the long axis is oriented perpendicular to the surface normal of the sample and parallel to the THz polarization, peak 2 with a domain where the long axis is oriented perpendicular to the surface normal and perpendicular to the THz polarization and peak 3 with a domain where the long axis is parallel to the surface normal. In the main text we focus on twin 3, which has the strongest signal.

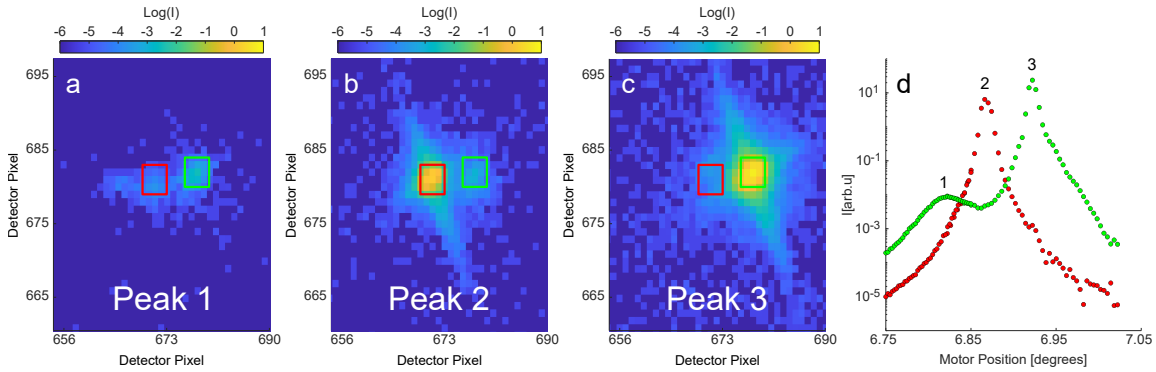

Fig. S2: **Twin domains in the angle scan of the (3,3,3) Bragg peak.** (a)-(c) Part of the detector image showing x-ray scattering for three different sample orientations close to the (3,3,3) Bragg condition. The red and green squares indicate the integration regions for the plots in (d). The sample orientations for (a), (b) and (c) correspond to the motor positions of peaks 1, 2 and 3 in (d) respectively. (d) The red and green circles are the integrated intensity in the corresponding red and green squares shown in (a), (b) and (c). The intensity is plotted versus the angle of one of the rotation motors which control the sample orientation.

THz Field Strength Dependence

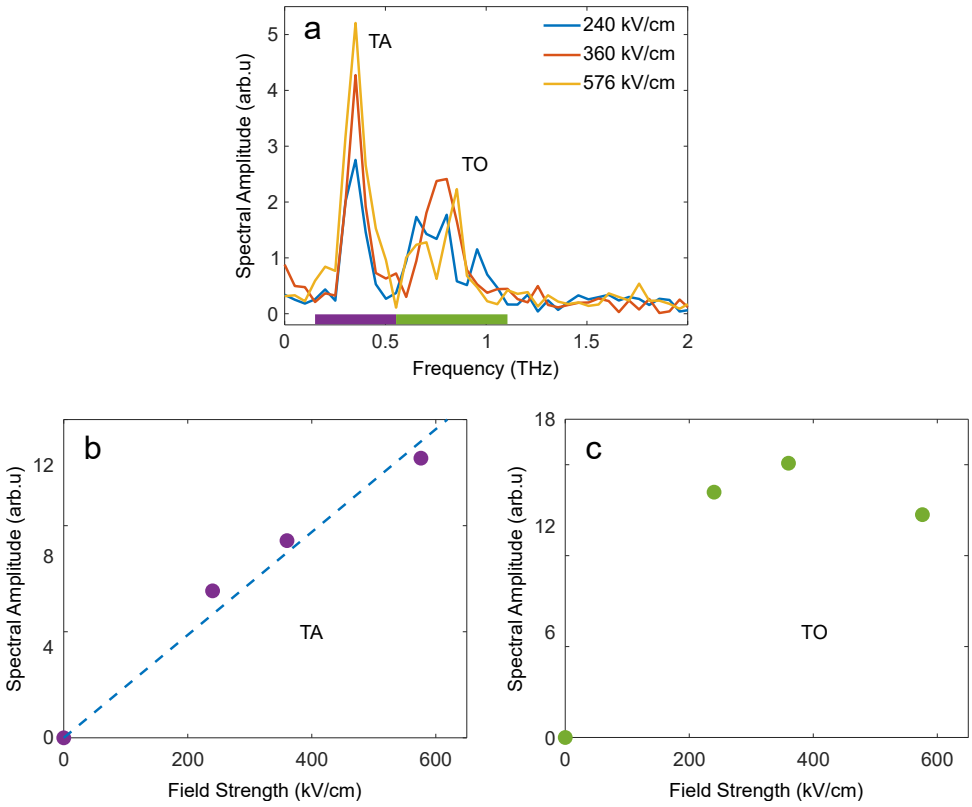

Fig. S3: **Fluence dependence of the high wavevector signal.** (a) Amplitude (absolute value) of the Fourier transform of the $\Delta I/I_0$ dynamics (e.g., main text Fig. 2b,c) at $\xi \approx 0.4$ versus frequency for three different THz field strengths at T=20 K. The traces show two distinct spectral features which we have identified as the TA and TO modes at this wavevector. The purple and green bars indicate the range over which we integrated to extract the total amplitude for each mode in (b) and (c). (b),(c) The spectrally integrated amplitude for the TA and TO respectively versus THz field strength. The blue line in (b) is a linear fit with both intercepts forced to 0.

In Fig. **S3** we extract the THz field strength dependence separately for the amplitudes of the TA and TO modes. Fig. **S3**b shows that the TA mode is predominantly linear with the field strength, providing further evidence that flexoelectric coupling dominates the polarization-strain interaction at the wavevectors we measure.

Negligible Pump Heating

Heating causes an increase in thermal diffuse scattering, which scales approximately linearly with the temperature gain[4]. Fig. **S4**a shows the x-ray scattering intensity versus pump-probe delay at $\xi \approx 0.4$ (blue line), along with the 'laser off' signal (orange line), where the pump is delayed by 100 nanoseconds relative to the x-ray probe. The 'laser off' signal is virtually indistinguishable from the signal with the pump blocked but enables fast switching between pump on and off on a pulse-by-pulse basis. These signals correspond to $E_{THz} = 576$ kV/cm, the highest THz field strength used in the experiment. Clearly, the signal level just before the arrival of the THz pulse (blue line before 0 ps) is very close to the level of the 'laser off' trace (orange line). This shows that the system returns to its initial state well before the next pump pulse arrives and combined with the low 120 Hz repetition rate, no average heating is expected. Furthermore, the coherent signal (blue line after 0 ps) oscillates around and decays towards the level of the orange trace, indicating no significant increase in thermal diffuse scattering. To better asses the possible rise in thermal diffuse scattering we show in Fig. **S4**b similar traces as in Fig. **S4**a from a region of the detector where the coherent oscillations are negligible. We chose this region to avoid the oscillations and better assess any possible thermal background increase. Comparing the mean intensity at $t > 0$ (blue trace) to that of the 'laser off' signal (orange trace) we estimate at most a rise of 6.5% in the thermal diffuse scattering, corresponding to a similar transient temperature increase. For 20 K this will lead to a ~ 1.3 K increase, which has no effect on our results.

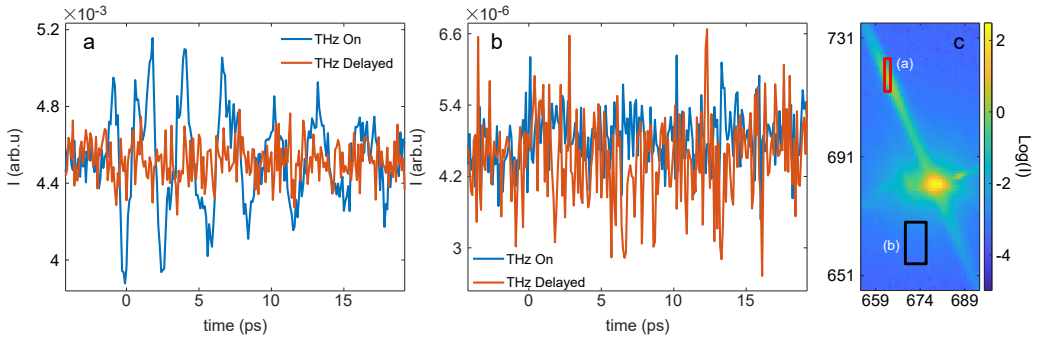

Fig. S4: **pump-probe and delayed signals.** (a) x-ray scattering intensity versus pump-probe delay at $\xi \approx 0.4$ (blue line). The orange trace shows the response of the same detector region with the THz pulses delayed by 100 nanoseconds relative to the x-ray probe. (b) The blue and orange lines are similar to the ones shown in (a), but taken from a different region of the detector where no coherent oscillations were observed, allowing us to identify the possible change in thermal diffuse scattering. (c) The detector image showing the regions where the signal in (a) (red rectangle) and (b) (black rectangle) were taken from.

References

[1] Lytle, F. W. X-ray diffractometry of low-temperature phase transformations in strontium titanate. *Journal of Applied Physics* **35**, 2212–2215 (1964).

[2] Hayward, S. A. & Salje, E. K. H. Cubic-tetragonal phase transition in $SrTiO_3$ revisited: Landau theory and transition mechanism. *Phase Transitions* **68**, 501–522 (1999).

[3] Kiat, J. M. & Roisnel, T. Rietveld analysis of strontium titanate in the Müller state. *Journal of Physics: Condensed Matter* **8**, 3471–3475 (1996).

[4] Xu, R. & Chiang, T. C. Determination of phonon dispersion relations by x-ray thermal diffuse scattering. *Zeitschrift für Kristallographie - Crystalline Materials* **220**, 1009–1016 (2005). URL `https://doi.org/10.1524/zkri.2005.220.12.1009`.